Original article

Nuclear Medicine Communications

Low-dose ^{90}Y PET/CT imaging optimized for lesion detectability and quantitative accuracy: a phantom study to assess the feasibility of pretherapy imaging to plan the therapeutic dose

Maryam Khazaee[a], Alireza Kamali-Asl[a], Parham Geramifar[b] and Arman Rahmim[c,d]

Objective **The overall aim of this work is to optimize the reconstruction parameters for low-dose yttrium-90 (^{90}Y) PET/CT imaging, and to determine ^{90}Y minimum detectable activity, in an endeavor to investigate the feasibility of performing low-dose ^{90}Y imaging in-vivo to plan the therapeutic dose in radioembolization.**

Materials and methods **This study was carried out using a Siemens Biograph 6 True Point PET/CT scanner. A Jaszczak phantom containing five hot syringes was imaged serially over 15 days. For 128 reconstruction parameters/ algorithms, detectability performance and quantitative accuracy were evaluated using the contrast-to-noise ratio and the recovery coefficient, respectively.**

Results **For activity concentrations greater than 2.5 MBq/ml, the linearity of the scanner was confirmed while the corresponding relative error was below 10%. Reconstructions with smaller numbers of iterations and smoother filters led to higher detectability performance, irrespective of the activity concentration and lesion size. In this study, the minimum detectable activity was found to be 3.28 ± 10% MBq/ml using the optimized reconstruction parameters. Although the recovered activities were generally underestimated, for lesions with activity concentration greater than 4 MBq/ml, the amount of underestimation is limited to − 15% for optimized reconstructions.**

Conclusion **^{90}Y PET/CT imaging, even with a low activity concentration, is feasible for depicting the distribution of ^{90}Y implanted microspheres using optimized reconstruction parameters. As such, in-vivo PET/CT imaging of low-dose ^{90}Y in the pretherapeutic stage may be feasible and fruitful to optimally plan the therapeutic activity delivered to patients undergoing radioembolization.** ***Nucl Med Commun*** **38:985–997**

Nuclear Medicine Communications 2017, **38**:985–997

Keywords: detectability, low-dose ^{90}Y PET/CT imaging, optimized image reconstruction, quantification, radioembolization

[a]Department of Medical Radiation Engineering, Shahid Beheshti University, [b]Research Center for Nuclear Medicine, Shariati Hospital, Tehran University of Medical Sciences, Tehran, Iran, [c]Department of Radiology and [d]Department of Electrical and Computer Engineering, Johns Hopkins University, Baltimore, Maryland, USA

Correspondence to Alireza Kamali-Asl, PhD, Department of Medical Radiation Engineering, Shahid Beheshti University, GC, Tehran 1983969411, Iran
Tel: + 98 21 2990 4227; fax: + 98 21 2243 1780; e-mail: a_kamali@sbu.ac.ir

Received 1 June 2017 **Revised** 24 July 2017 **Accepted** 10 August 2017

Introduction

Selective internal radiotherapy (SIRT), also known as liver radioembolization, is a promising technique for patients with primary or metastatic liver cancer. In this technique, yttrium-90 (^{90}Y) radionuclides are coated with resin or glass microspheres and are locally injected near the tumor by catheterization [1].

Some characteristics of ^{90}Y make this radionuclide an ideal isotope for the treatment of liver lesions in the radioembolization technique. In particular, ^{90}Y is an almost pure β emitter (99.98%) and has a long half-life of 64.2 h [2]. The mean and maximum energy of emitted particles are 0.94 and 2.28 MeV, respectively, providing mean (maximum) tissue penetration of 2.5 mm (10 mm) [2,3].

Although the application of ^{90}Y in radioembolization has increased, current methods for calculating the optimized therapeutic activity are rudimentary. The body surface area (BSA) method and the partition model are two common techniques [3,4]. Imaging through technetium-99m macroaggregated albumin (^{99m}Tc-MAA) as the radionuclide surrogate is considered to be the best pretherapeutic dosimetry technique in clinics [3]. However, this method leads to significant complications. Specifically, the distribution of ^{90}Y is assumed to match that of a different radiopharmaceutical. Nonetheless, the in-vivo distributions of these two radionuclide may differ because of several factors including differences in catheter placement and injection techniques, and different physical characteristics such as nonidentical particle sizes, different flow between ^{99m}Tc-MAA and ^{90}Y microspheres, and different energy radiation of ^{90}Y (bremsstrahlung emission) compared with that of ^{99m}Tc, resulting in different quantitative accuracies [5–7].

DOI: 10.1097/MNM.0000000000000742

In any case, a precise activity distribution is required to perform accurate dosimetry in the pretherapy stage using low-dose ^{90}Y injection and to ultimately calculate the optimized therapeutic activity for radioembolization. In this respect, we propose a novel approach based on low-dose ^{90}Y injection in the pretherapy stage and to directly make use of PET/CT imaging of the real activity distribution in-vivo to optimize the injected therapeutic ^{90}Y activity for SIRT. It should be noted that in this technique, in the first place, a small fraction of the therapeutic dose should be injected to the patient. Then, the sufficient required activity would be determined using PET/CT imaging of the same radionuclide. Subsequently, the residual of the required activity could be injected into the patient using the same catheter position and injection technique. In this scheme, the first injected part of the activity, used to perform patient-specific dose planning, is considered the initial fraction of the therapeutic dose.

SPECT/CT and PET/CT scanners are two imaging modalities used to determine the radionuclide distribution [8,9]. To estimate the activity distribution of ^{90}Y radiopharmaceuticals, SPECT/CT imaging is possible by bremsstrahlung radiograph emissions [10]. Although reconstruction algorithms are being improved [10–12], the images suffer from unreliable quantification and insufficient spatial resolution. As such, further research is essential to quantitatively evaluate the dose distribution on the basis of SPECT/CT imaging [10,11,13]. A recent study reported promising results for bremsstrahlung imaging of ^{90}Y using pinhole collimators [13].

The small positron branching ratio (the ratio between the numbers of emitted positrons to electrons) that is attributed to the zirconium-90 transition, following its β decay, provides the possibility of ^{90}Y PET imaging. However, this results in weak signals from ^{90}Y PET imaging compared with usual PET tracers. In 1938, Arley and Moller [14] theoretically investigated this transition. Greenberg *et al.* [15] reported a positron branching ratio of $3.6 \pm 0.9 \times 10^{-5}$ for ^{90}Y for the first time. The most recent positron branching ratio determined by Selwyn *et al.* [16] was equal to $3.187 \pm 0.47 \times 10^{-5}$.

Different studies have shown the feasibility of using PET/CT for depicting the distribution of implanted ^{90}Y microspheres [17–21]. The associated quantitative analysis can potentially provide a solid foundation for accurate dosimetry. These studies mainly focused on lesions with high activity concentrations (generally several MBq/ml). However, the activity concentration in the pretherapy stage should be limited. Accordingly, it is essential to first investigate the minimum detectable activity (MDA) of low-dose ^{90}Y using PET/CT imaging to determine the feasibility of lesion detectability incorporating pretherapy dose, which is an important component of the present work.

The PET/CT imaging of low-dose ^{90}Y results in a limited number of true coincidences even over a scan duration of 30–45 min/bed position. Consequently, the detection and quantification performance can especially depend on the reconstruction parameters, lesion size, and activity concentration. In this study, the impact of aforementioned parameters on detectability and the quantification assessment is explored.

The study aims to (a) optimize reconstructions for low-dose ^{90}Y PET/CT imaging to enable more accurate quantification and higher detectability performance; (b) determine ^{90}Y MDA in an endeavor to investigate the feasibility of applying low-dose ^{90}Y in-vivo imaging for estimating the therapeutic dose in SIRT toward more accurate treatment planning; and (c) evaluate quantification and detectability performance for the defined optimized reconstructions in an LSO-based PET/CT imaging system as a function of both hot-sphere size and activity concentration. We emphasize that past work, in different imaging contexts, has shown that detectability versus quantification may be optimized distinctly [22–25], given the different underlying tasks, and as such, we also aim for distinct optimization.

Materials and methods

PET/CT acquisition setup

The study was carried out using a Siemens Biograph 6 True Point PET/CT scanner (Siemens, Erlangen, Germany), equipped with resolution recovery, also known as resolution modeling or PSF modeling [26,27]. The coincidence window was set to 4.5 ns and the patient port aperture was 70 cm. In all studies, low-dose CT scans were obtained before PET scans and used for lesion localization, attenuation, and scatter corrections.

Phantom study

A Jaszczak phantom containing five hot syringes (internal diameters 30.5, 22, 17.5, 13.65, and 9.15 mm) was filled with a uniform concentration of ^{90}Y to achieve a 40 : 1 syringe-to-background ratio (SBR). SBR was selected so that a high tumor uptake in comparison with the background was realized [28]. The volume of the phantom was 3 l and it was initially filled with an activity concentration of 180 kBq/ml of ^{90}Y chloride. The entire phantom was centered in the field of view (FOV) of the PET scanner and the images were acquired at a single-bed position. Detector events of PET/CT acquisition were collected for 45 min and the phantom was imaged serially 11 times over 15 days.

PET/CT measurement

For the Siemens Biograph 6 PET/CT scanner, ^{90}Y is not provided on the isotope list at the scanner console. Thus, the ^{86}Y template was used as an alternative isotope for the acquisition procedure. This isotope has different tracer parameters from those of ^{90}Y. Accordingly, the

activity concentrations were not reported on the basis of PET/CT images because of electron or positron emission of ^{90}Y. To account for this discrepancy, a correction factor was applied to the reconstructed data on the basis of ^{86}Y measurements to achieve quantitative results according to those of ^{90}Y [21]. This correction factor was derived from the intraframe decay correction for each isotope (as expressed, e.g., in Goedicke and colleagues [21,29]):

$$\mathrm{DC(I)}=\frac{T_{\mathrm{N}}(\mathrm{I})}{1-\exp[-T_{\mathrm{N}}(\mathrm{I})]}, \quad (1)$$

where $T_{\mathrm{N}}(\mathrm{I})=\ln(2)\times\frac{T_{\mathrm{A}}}{T_{1/2}(\mathrm{I})}$, $T_{1/2}(\mathrm{I})$ is the half-life of the isotope (I), and T_{A} is the acquisition time in the same unit as $T_{1/2}(\mathrm{I})$. According to this formula, the correction factor can be expressed as the quotient of correction terms for each isotope, that is, DC (^{90}Y)/DC (^{86}Y):

$$\text{Correction factor}\,(^{86}\mathrm{Y}\rightarrow{}^{90}\mathrm{Y})=\frac{T_{1/2}(^{86}\mathrm{Y})}{T_{1/2}(^{90}\mathrm{Y})}\times\frac{1-\exp[-T_{\mathrm{N}}(^{86}\mathrm{Y})]}{1-\exp[-T_{\mathrm{N}}(^{90}\mathrm{Y})]}. \quad (2)$$

For the acquisition time of this study (45 min) and the half-life of ^{86}Y (48 min) [21], a factor of 0.74 should be multiplied by the reconstructed data to obtain accurate results for ^{90}Y.

Furthermore, it should be noted that the measured activity of ^{90}Y is a result of electron energy depositions, whereas PET/CT image is formed on the basis of photons created through positron annihilations. As such, for the activity concentrations based on the PET/CT reconstructed images, the positron branching ratio of ^{90}Y is also considered.

The linearity of PET/CT imaging was evaluated for the task of quantifying ^{90}Y activity. The initial activity concentration in hot syringes started from 7.23 MBq/ml decreasing to 0.19 MBq/ml. The activity concentrations for 11 different time-points during 15 days of imaging are shown in Table 1.

True activity concentrations in each time-point were computed on the basis of the physical decay and the results were compared with the activity concentrations measured from PET/CT images. As shown in Fig. 1a, a linear fit was applied to the two sets of the achieved results to examine the relationship between the true and the measured activity concentrations, and to evaluate the saturation or biasing effects. The percentage of the relative errors along the activity range is shown in Fig. 1b. It should be noted that although the total injected activity in SIRT is known and locally stable, the FOV of the PET scanner may not totally cover the application region. Consequently, calibration of the scanner is required to perform precise image-based dosimetry.

The LSO scintillation crystals used in our Siemens Biograph PET/CT scanner have intrinsic radioactivity. Lutetium-176 (^{176}Lu) emits electrons, followed by one or more γ-ray emissions and true counts are detectable even without the presence of radioactivity in PET FOV [30,31]. These true and random counts, as a result of the natural radioactivity, lead to an intrinsic background [30,32] that can mask weak signals. Moreover, ^{90}Y bremsstrahlung emissions also contribute toward the background signal. This portion of the background signal depends on the total activity concentration of ^{90}Y after injection, the scanned object, as well as attenuation correction and reconstruction algorithms.

To calculate the background signal, we plot the activity concentration in the hot syringes without background subtraction versus time. The extrapolation shows an offset that is equal to this background signal [33] as shown in Fig. 2.

Reconstruction method and parameters

In this study, four OSEM reconstruction parameters were adopted: the number of iterations (N_{i}), the number of subsets per iteration (N_{s}), the smoothing filters, and the application of the resolution recovery technique (HD). The attenuation-corrected and scatter-corrected sinograms were applied using low-dose CT images. The applied postsmoothing filters include all-pass, as well as Gaussian filters with full-width at half-maximum (FWHM) values of 3, 5, and 8 mm.

We consider a set (A) of 13 values below as representing the product of N_{i} and N_{s} values:

A = {4, 8, 12, 14, 16, 21, 24, 28, 32, 42, 56, 63, 84}.

The number of evaluated reconstruction parameters is determined by values of set A, the number of smoothing filters, and the application of HD, leading to 128 configurations. To investigate the impact of increasing the iteration on the detectability and quantitative accuracy, 1–4 iterations were considered. A maximum of four iterations was selected to restrict noise amplification.

For each activity concentration, the raw data are reconstructed on the basis of the described variations, and the impacts of reconstruction parameters on the detectability performance and quantitative estimation were evaluated.

Table 1 Activity concentrations in syringes and phantom backgrounds

Elapsed time (h)	0	24	72	96	120	144	168	192	240	288	336
Activity concentration in syringes (MBq/ml)	7.23	5.58	3.32	2.56	1.98	1.53	1.18	0.91	0.54	0.32	0.19
Activity concentration in phantom (MBq/ml)	0.18	0.14	0.08	0.06	0.05	0.04	0.03	0.02	0.01	0.008	0.004

Fig. 1

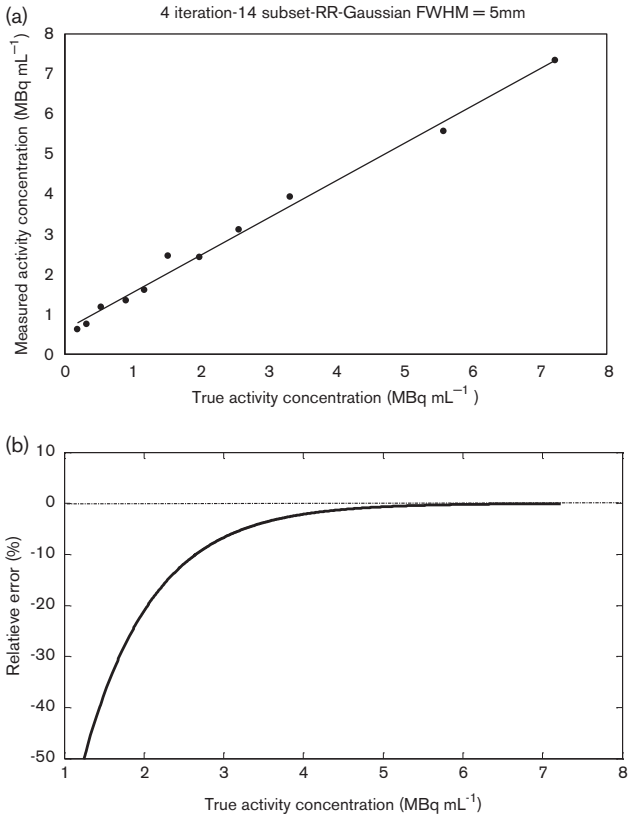

True activity concentrations versus measured activity concentrations (a) and the associated relative errors (b). FWHM, full-width at half-maximum.

Fig. 2

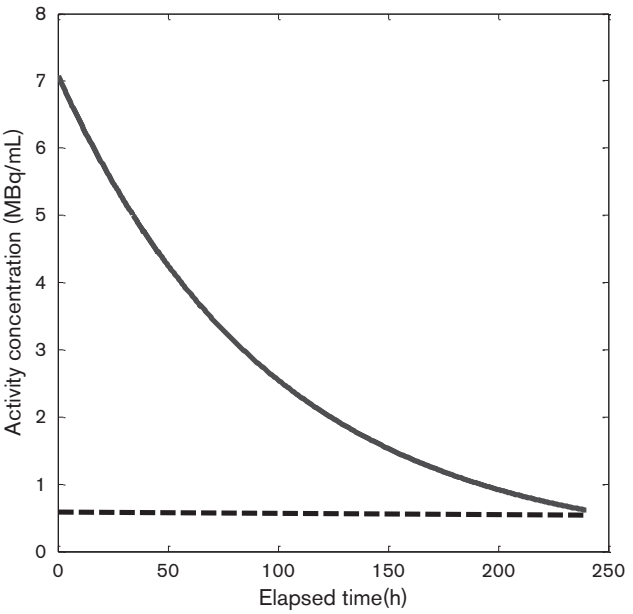

The average of the measured activity concentrations in hot syringes using PET/CT, without background subtraction versus time.

PET/CT images were reconstructed both with PSF modeling (TrueX reconstruction) and without PSF modeling (three-dimensional iterative OSEM algorithms). Further postprocessing of datasets as well as visualization of the results were performed using Matlab (R2008b; The Mathworks, Nattick, Massachusetts, USA).

Data analysis

To evaluate the impact of reconstruction parameters on the detectability performance and quantitative accuracy, the contrast-to-noise ratio (CNR) and activity recovery within predefined volumes of interest (VOIs) were calculated for various reconstruction parameters.

Detectability

As the small positron branching ratio of ^{90}Y results in weak signals for this radionuclide compared with the common PET tracers, lesion detection with ^{90}Y PET imaging has been the subject of some research [28,30,34].

It should be noted that higher lesion-to-background ratios correspond to enhanced image contrast. At the same time, statistical noise levels also play an important role in the detection performance of lesions incorporating ^{90}Y and they should be considered as well. Consequently, the CNR index based on the following formula represents a more thorough metric to assess detectability performance using the Rose criterion. On the basis of the Rose criterion, an object is considered discernible when the calculated CNR values exceeds ~5 [35]:

$$\mathrm{CNR}=\frac{\mathrm{C_{lesion}}-\mathrm{C_{background}}}{\sigma_{\mathrm{background}}}, \quad (3)$$

where C_{lesion} and $C_{\mathrm{background}}$ denote the lesion and the background signals, respectively, and $\sigma_{\mathrm{background}}$ is the variability in background intensity [35].

As an alternative to performing extensive multiple-noise realization measurements, we follow an approach similar to Carlier *et al.* [28]. Accordingly, 20 regions of interest (ROIs), each containing 32 voxels, were chosen randomly in the background region. These background ROIs were selected in such a way that they are at least three voxels away from each other and at least four voxels away from phantom boundaries. Hence, the correlations between ROIs were avoided and various statistically independent ROIs were implemented [28,36]. The background noise for each of the selected ROIs, σ_B^j, was calculated on the basis of the following formula [28]:

$$\sigma_B^j=\sqrt{\frac{1}{32}\sum_{i=1}^{32}(A_{\mathrm{average}}-A_i)^2}, \quad (4)$$

where $A_{average}$ is the average activity inside each ROI and A_i represents the activity of each voxel in the reconstructed image. The total background noise of the reconstructed image was measured on the basis of the 20 defined ROIs in the background region of the aforementioned transverse slice as follows [28]:

$$\sigma_B = \frac{1}{20}\sum_{j=1}^{20}\sigma_B^j. \quad (5)$$

The transverse slice used to measure the background noise was selected in such a way to align with sphere centers that were chosen for data analysis. The above measure provides a nearly equivalent measure of variability for a signal achieved from a single voxel [28] for a lesion consisting of N voxels, Eq. (3) is then modified as follows [37]:

$$\mathrm{CNR} = \frac{C_{lesion} - C_{background}}{\sigma_{background}} \times \sqrt{N}. \quad (6)$$

The shapes of the filled part of the syringes are close to the circular-shaped objects. Bright *et al.* [38] assessed various contexts of simulated noisy micrographs based on human observers. They recommended that circular-shaped objects were detectable if the corresponding CNR exceeded 8. Therefore, the limit of CNR as a detectability threshold is modified to be greater than 8 in this work. To find the best reconstruction parameters for detectability, the CNR parameters were measured for all 128 configurations in the first day of imaging and the achieved results were compared for all the syringes.

Quantification accuracy

The activity measured on the first day of imaging was used to calculate the true activity concentrations. Activity concentrations at the following imaging time-points were determined by taking the physical decay of ^{90}Y into account as illustrated in Table 1. The measurements of activity concentrations were associated with uncertainties limited to −15%, which was because of uncertainties in volume and activity calculations using the Capintec-CRC-25R dose calibrator (Capintec Inc., Ramsey, New Jersey, USA) [39].

In this study, the reconstructed PET and corresponding CT data at each imaging time-point were used to delineate five hot syringes in the phantom. The VOIs are defined on the basis of a determined percentage of the maximum PET intensity. The percentage was chosen in such a way that we achieved the highest conformation between the volumes measured from CT and PET images. The mean intensity of all voxels inside this VOI defines the activity concentration in the corresponding volume that is associated with the SD. The accuracy of this measured activity concentration is indicated as the percentage difference between the expected and the measured values. To measure the precision of the obtained data, SD is indicated in terms of the mean activity concentration. This parameter, which is also referred to as the coefficient of variation (CoV), is calculated as follows [40]:

$$\mathrm{CoV}(\%) = \frac{\mathrm{SD}}{\mathrm{Mean}} \times 100. \quad (7)$$

The accuracy and CoV of the reconstructed activity concentrations for 11 different time-points for 15 days are measured for all aforementioned reconstruction parameters.

The PET-reconstructed activity concentrations in each syringe for all the imaging time-points are divided by the calculated activity concentration as follows:

$$\text{Recovery coefficient} = \frac{\text{Measured concentration}}{\text{True concentration}} \times 100. \quad (8)$$

The percentage of recovery coefficient (RC) is plotted for syringes with 9.15 and 30.5-mm diameters for different imaging time-points. The activity concentrations in each syringe measured were compared with the calculated values (true activity concentration) to evaluate the quantitative accuracy of the segmented VOIs. The difference between activity concentrations in the reconstructed VOIs and the true activity concentration at each imaging time-point was calculated.

Results

Hardware linearity and background assessment

The linearity of the PET/CT scanner and the activity calibration method for ^{90}Y imaging was evaluated. The calculated values were compared with the measured activity concentrations derived from the PET/CT images. This is shown in Fig. 1.

As the linear fit illustrates, there was no saturation or biasing effect. Moreover, the applied corrections applied to the raw data to accurately quantify the activity concentration were confirmed. True activity concentrations (A_{true}; MBq/ml) are related to the measured activity concentrations ($A_{measured}$; MBq/ml) through the following equation:

$$A_{measured} = 0.9099 \times A_{true} + 0.6864 \left(R^2 = 0.9918\right). \quad (9)$$

For activity concentrations more than 2.5 MBq/ml, the relative errors are below 10%, whereas this quantity is below 2% for activity concentrations more than 5 MBq/ml in all the measurements. Furthermore, the average of the measured activity concentrations in hot syringes using PET/CT images is plotted against time throughout the imaging period, without background subtraction, and an exponential fit is applied to these points. A correlation coefficient of 0.999 was found between the measured points and the calculated exponential fit, and the plot has an offset equal to 0.67 MBq/ml (the dash line), which can be considered the background signal.

Fig. 3

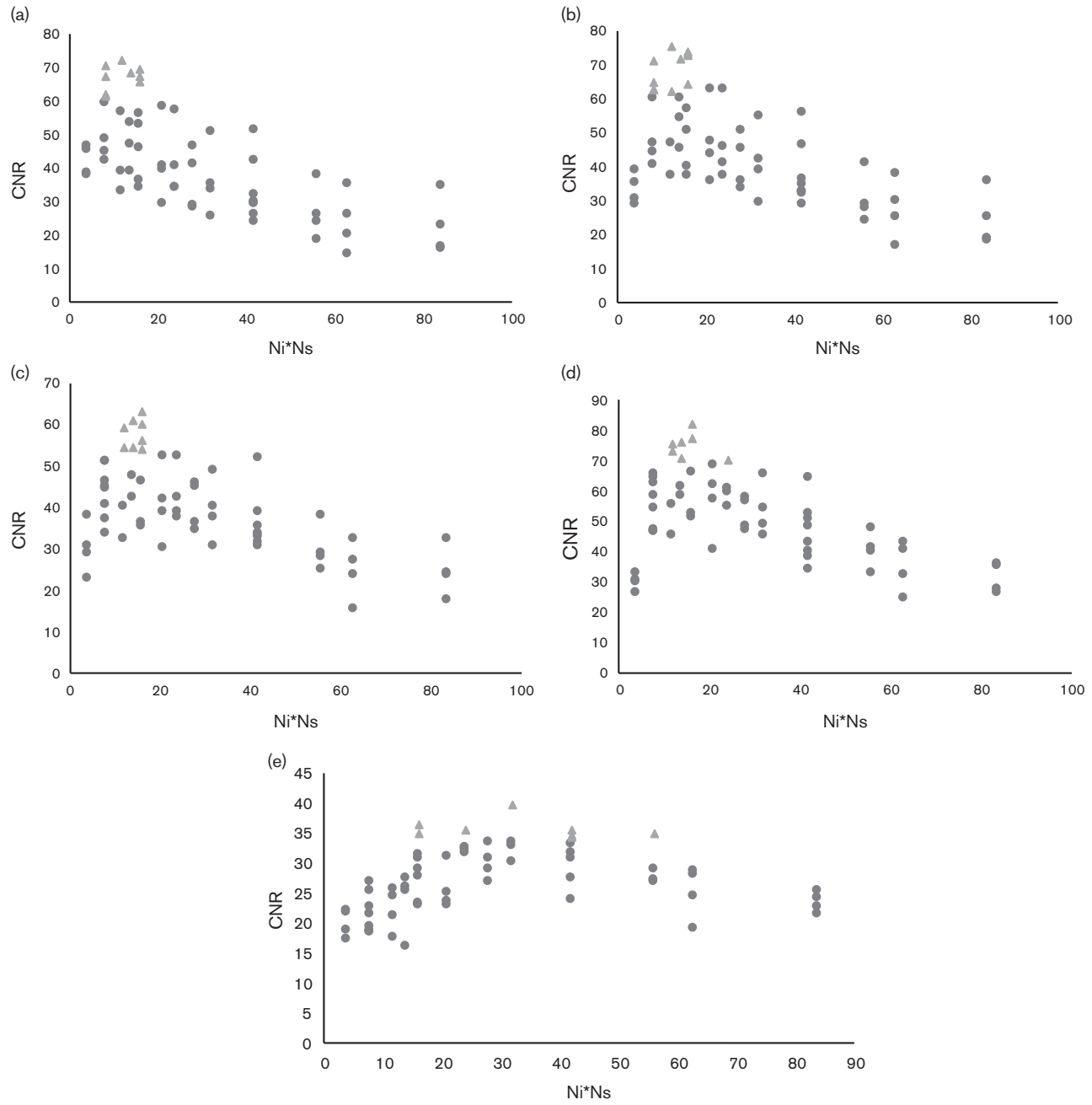

The CNR values for various reconstruction parameters for (a) 30.5-mm, (b) 22-mm, (c) 17.5-mm, (d) 13.6-mm, and (e) 9.15-mm diameter syringes (triangular points are the top CNR values corresponding to the highest detectability). CNR, contrast-to-noise ratio; N_i, number of iterations; N_s, number of subsets.

However, the average activity concentration in cold spheres (a sphere without activity in the phantom) for all the 11 measurements is 0.70 MBq/ml, which is within 4% of the value calculated with the fitting offset. As such, for the activity range in this study, the contribution of ^{90}Y bremsstrahlung emission toward the background is less than intrinsic background because of the ^{176}Lu. At the same time, it is highly recommended to subtract the background signal from the measured activity concentration.

The optimized reconstruction parameters

Detectability

In general, it is observed that similar reconstruction parameters result in identical CNR values for all the syringes, except for the smallest one.

As is evident from Fig. 3, the CNR value decreases significantly for reconstructions with iterations more than 42. The image noise increases as the number of iterations

increases, and consequently, the visual performance decreases. Thus, for a higher detectability performance, it is essential to use reconstruction parameters with lower numbers of iterations.

Quantitative accuracy

For each set of the reconstruction parameters, the activity concentrations (in MBq/ml) for various hot, cold, and background regions are calculated on the basis of the reconstructed PET/CT images. To find the optimized reconstruction parameters of quantitative accuracy, CoV and accuracy values for all activity concentrations and reconstruction parameters are considered.

In general, a smaller CoV (SD compared to the mean value) shows higher precision. In this work, reconstruction parameters that estimate activity concentration with high precisions and accuracy values are proposed.

As shown in Fig. 4, the application of smoother filters results in lower CoV and improved precision. Consequently, Gaussian smoothing filters with 5 and 8-mm FWHM are preferred in terms of quantitative accuracy.

As the number of iterations is increased, the estimated values for the activity concentration also increase until their curve reaches a plateau, as can be seen in Fig. 5. Further increase in the number of the iterations would not only alter the value of the estimated activity concentration but also amplifies the noise signal. Consequently, the reconstruction parameters that have the iterations in the beginning of the plateau region improve the accuracy of the quantitative evaluation.

Evaluating the impact of reconstruction parameters on *Minimum detectable activity*

The detectability performances of syringes with the largest and the smallest diameter for the optimized reconstruction parameters are shown in Fig. 6. Reconstructions with smaller number of iterations and smoother filters lead to higher detectability performance, irrespective of activity concentration and syringe size.

Generally, decreasing the syringe size and activity concentrations degrades the CNR values.

In this analysis, MDA is determined as the activity concentration for the smallest volume so that the associated CNR is greater than 8. As presented in Fig. 7, all the hot volumes that are reconstructed using the optimized parameters are detectable with activity concentrations higher than 3.28 ± 10%MBq/ml, irrespective of their diameter. Therefore, the MDA is calculated to be 3.28 ± 10%MBq/ml.

As the CNR decreases slowly with the radioactive concentration and the background noise is considerably high (Fig. 8), a qualitative subjective assessment is performed by an expert physician. As can be expected, smaller objects are associated with higher MDA, irrespective of their activity concentration. Using the optimized reconstruction parameters, all the hot volumes are visible for activity concentrations higher than 3.33 MBq/ml.

Partial volume effect and activity recovery

We have shown that the hot syringe with the largest diameter is not affected by the partial volume effect (PVE). Thus, to evaluate the RC when the count statistics are decreased, the RC is plotted against the imaging time-points in Fig. 9a. Furthermore, to assess the PVEs, the RCs of the smallest syringe are shown in Fig. 9b for different activity concentrations on the first day of imaging.

The RCs for all hot syringes on the first day of imaging are shown in Fig. 9c. The trends for RCs are identical for all syringes. The application of Gaussian filters with an 8-mm FWHM in the reconstruction parameters results in a more significant underestimation of the activity concentration compared with the results obtained with a 5-mm FWHM. Accordingly, smoother filters decrease the RC and the reconstructed activities would be more underestimated. In addition, the impact of PVE is more significant for smaller objects; thus, a steady decline is observed for RCs for syringes with a diameter less than 30.5 mm.

The calibration value is calculated by dividing each measured activity concentration by the ^{90}Y positron branching ratio [33] and including the decay correction factor (Eq. 2). The value of activity concentration in the central cold insertion is considered the true background concentration and is subtracted from all the measured activity concentrations in hot syringes.

The accuracy of reconstructed activity concentrations in the syringes at each imaging time-point for the optimized reconstruction parameters are calculated. The relative differences between the expected and the measured activity concentrations are averaged over the five syringes as presented in Fig. 10. Dashed lines indicate a ±15% tolerance, showing expected uncertainties associated with the 'true' values.

For activity concentrations higher than 4 MBq/ml, the relative differences for the reconstructions with four

Fig. 4

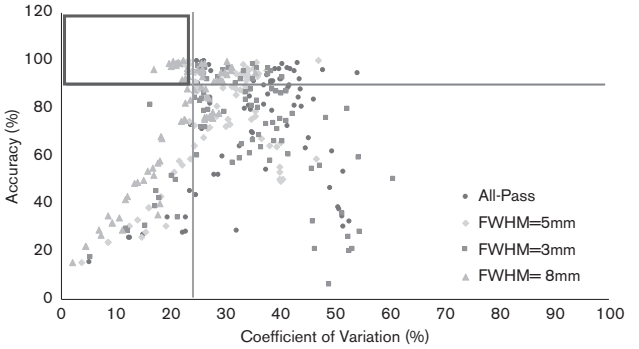

Accuracy and coefficient of variation (CoV) for all the reconstructed activity concentrations. The box indicates the suggested reconstruction parameters. FWHM, full-width at half-maximum.

Fig. 5

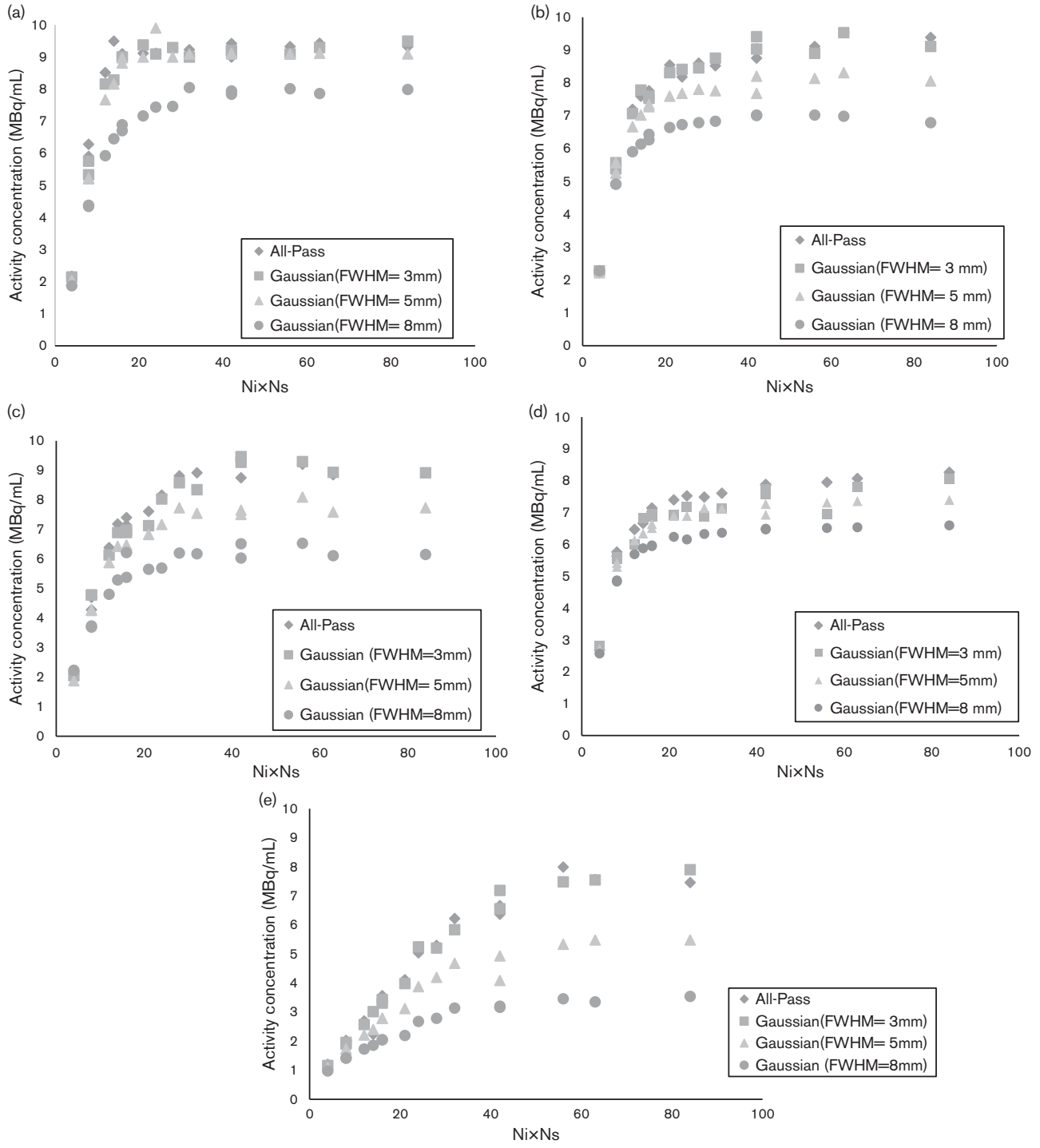

Measured activity concentration versus various number of subiterations for syringes with a diameter of 30.5 mm (a), 22 mm (b), 17.5 mm (c), 13.65 mm (d), and 9.15 mm (e). FWHM, full-width at half-maximum; N_i, number of iterations; N_s, number of subsets.

iterations and 14 subsets (4i14s), 2i21s, and 2i14s, using the Gaussian filter with 5-mm FWHM, are limited to −15%. For activity concentrations below 2 MBq/ml, the underestimation is between −20 and −60% for the optimized reconstructions. In the current study, the non-TOF Siemens system was utilized, and the estimated values of activity concentration in hot syringes and background are in agreement with the research by Willowson *et al.* [39].

Fig. 6

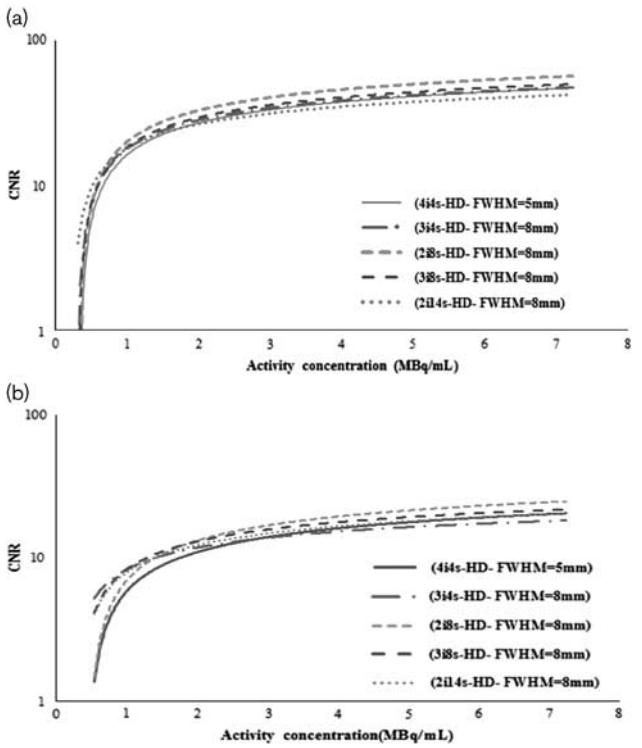

CNR versus true activity concentration in a syringe with (a) 30.5 mm of diameter and (b) 9.15 mm of diameter for different optimized reconstruction parameters. CNR, contrast-to-noise ratio; FWHM, full-width at half-maximum.

Fig. 7

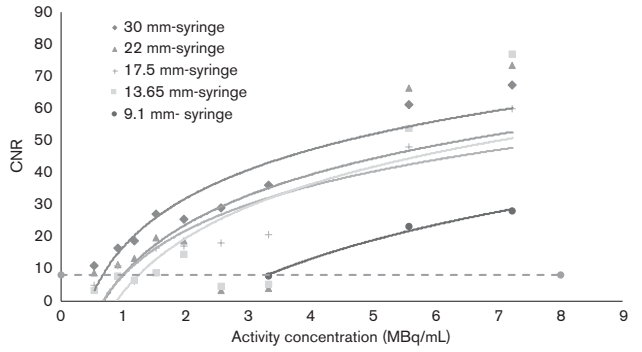

Plots, and lines of best fit, for CNR in hot syringes of various diameters versus activity concentration for the optimized reconstruction parameters. CNR, contrast-to-noise ratio.

Discussion

Potential for a new approach

The therapeutic activity of ^{90}Y to be injected to patients in radioembolization, which is calculated on the basis of the partition model, suffers from an associated intrinsic uncertainty because of the assumption that the spatial distribution of ^{90}Y microspheres is identical to ^{99m}Tc-MAA surrogates [5–7]. In this study, we proposed a novel framework to investigate the feasibility of applying low-dose ^{90}Y in-vivo PET/CT imaging to depict the radionuclide spatial distribution using the optimized reconstructions.

It should be noted that in this technique, dosimetry at the pretherapeutic stage would be viable only if intraoperative PET/CT imaging in SIRT is possible. As such, in the first place, a fraction of the therapeutic dose could be injected to the patient. Then, the sufficient required activity could be determined using PET/CT imaging. Subsequently, the residual of the required activity could be injected to the patient in the same session of therapy. In this scheme, the first injected part of the activity, used to perform patient-specific dose planning, is considered the initial fraction of the therapeutic dose.

In addition, in the partition model, the distributions of microspheres in tumorous and healthy compartments of the liver are presumed uniform, although various studies have shown that microspheres prefer to build up inhomogeneous clusters at the tumor periphery [4,41–43]. As such, quantitative analysis and voxel dosimetry are ideally used to estimate the dose distribution in tumorous and nontumorous tissues, resulting in patient-specific dose planning to estimate the therapeutic dose in SIRT in the pretherapy stage.

Optimized reconstruction parameters

Although several studies have investigated the spatial distribution of the ^{90}Y microsphere within the liver and adjacent organs [18,20,29], to the best of our knowledge, low-dose ^{90}Y PET/CT imaging has not been used at the pretherapy stage to perform accurate dosimetry, given the low activity concentration. It must be noted that the aforementioned works focused primarily on the quantification and detection of tumors following radioembolization. Accordingly, the associated activity concentrations in lesions were within the therapeutic range. However, in this work, we attempted to assess the feasibility of pretherapeutic imaging of lesions incorporating lower amounts of radiotracers compared with the therapeutic dose.

Furthermore, the foregoing studies were limited to merely one or two reconstruction parameters, whereas we considered a range of reconstruction parameters for optimized task performance.

Subsequently, in the present study, PET/CT imaging of ^{90}Y was performed for various ($n = 11$) time-points spanning 15 days during which the activity concentrations in hot syringes decayed from 7.23 to 0.19 MBq/ml. The experimental results for 128 reconstruction configurations were compared to ascertain optimized reconstructions for tasks of detectability and quantification.

It was found that reconstruction with iteration numbers less than 42 resulted in higher detectability performance. By

Fig. 8

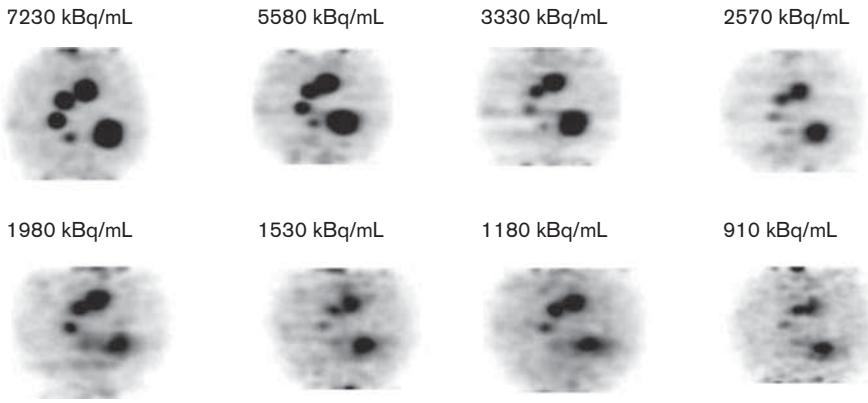

Transverse PET/CT slice of the Jaszczak phantom, crossing all five hot syringes (internal diameters of 30.5, 22, 17.5, 13.65, and 9.15 mm) for eight imaging time-points using the optimized reconstruction parameters.

comparison, higher iterations lead to more accurate quantitative assessments of activity concentration on the basis of PET/CT imaging irrespective of lesion size and activity concentration. The results are consistent with previous work in this context, where an identical SBR was selected as the figure of merit [28]. In that study, two reconstruction parameters (with one and three iterations) were compared and it was shown that one iteration provided more appropriate performance in terms of detectability, whereas for a more precise quantification, three iterations were required.

As shown in Fig. 3, the following reconstruction parameters are suggested for optimized lesion detectability in PET/CT imaging of ^{90}Y:

$N_i = 4$, $N_s = 4$, HD, and Gaussian (FWHM = 5 mm).

$N_i = 3$, $N_s = 4$, HD, and Gaussian (FWHM = 8 mm).

$N_i = 2$, $N_s = 8$, HD, and Gaussian (FWHM = 8 mm).

$N_i = 3$, $N_s = 8$, HD, and Gaussian (FWHM = 8 mm).

$N_i = 2$, $N_s = 14$, HD, and Gaussian (FWHM = 8 mm).

At the same time, although a higher number of iterations improves quantification performance, it amplifies noise and increases the number of false positives in lesions that are small or contain low concentrations because of the impact of ^{176}Lu background [28]. As such, increasing the number of iterations improves quantitative accuracy, but should be restricted above a given threshold. This result is in agreement with the data reported by Willowson *et al.* [39].

In this study, as concluded from Figs 4 and 5, the following parameters showed optimized performance for accurate quantitative PET/CT imaging of ^{90}Y.

$N_i = 2$, $N_s = 14$, HD, and Gaussian (FWHM = 5 mm).

$N_i = 4$, $N_s = 14$, HD, and Gaussian (FWHM = 5 mm).

$N_i = 2$, $N_s = 21$, HD, and Gaussian (FWHM = 5 mm).

$N_i = 3$, $N_s = 14$, HD, and Gaussian (FWHM = 8 mm).

$N_i = 4$, $N_s = 14$, HD, and Gaussian (FWHM = 8 mm).

$N_i = 2$, $N_s = 21$, HD, and Gaussian (FWHM = 8 mm).

These results are consistent with a previous work in this context by Goedicke *et al.* [21] in which the product of the iterations and subsets of the optimized reconstruction parameters were equal to or larger than those of the standard reconstruction parameters. The optimized number of iterations and subsets in the aforementioned study are still different from the results in the present study because of the use of distinct scanners.

These reconstruction parameters markedly improve detectability performance and quantitative assessments. In conclusion, two different sets of optimized reconstructions are introduced for detectability and quantitative accuracy. This is consistent with observations in other imaging areas that a set of parameters that optimize detectability do not necessarily optimize quantification and vice versa [22–25].

Minimum detectable activity

Lesions containing ^{90}Y have low count rates and signals, and as such, the background signal plays an important role in detection and quantification. The background signal is a result of the intrinsic radioactivity performance of ^{176}Lu in the scintillation crystals (LSO, LYSO) utilized in some PET scanners [30,31]. The other portion of the background signal is because of the bremsstrahlung photons from electrons slowing down in the phantom. The impact of the background signal depends on the reconstruction algorithm, the total activity concentration of ^{90}Y, and the geometry of the scanned object.

It is observed that lesion uptake with activity concentrations below a specific threshold could be masked by the background signal. In this work, this threshold was found

Fig. 9

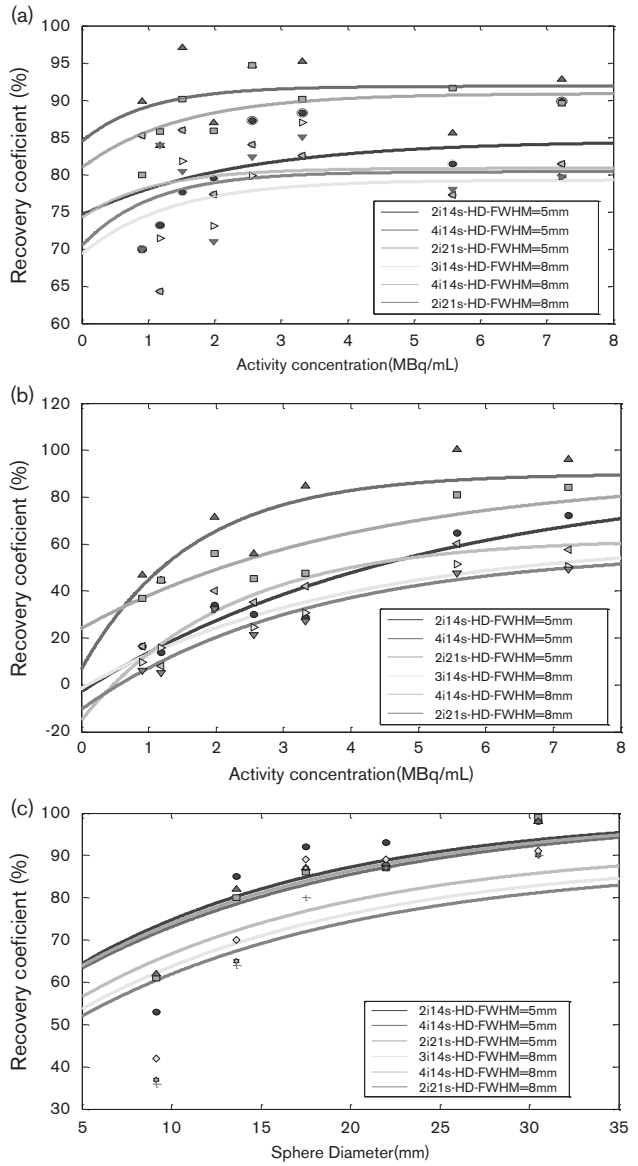

Recovery coefficient for (a) 30.5-mm diameter syringe, (b) 9.15-mm diameter syringe at different activity concentrations, and (c) in hot syringes of different diameters on the first day of imaging considering the optimized reconstruction parameters for quantification accuracy. FWHM, full-width at half-maximum.

to be 3.28 ± 10% for lesions with 9.1-mm diameter, reconstructed using the optimized parameters. As shown in Table 2, for larger lesions, the threshold decreases markedly. For activity concentrations below this threshold, the ^{176}Lu signal has a significant contribution of random coincidences in the background signal [28]. Resulting in multiple false-positive foci in the reconstructed image with moderate intensity, and the number of these false-positive foci increases for lower activity concentrations. Accordingly, the required activity concentration for treatment planning corresponds to the lesion size.

Fig. 10

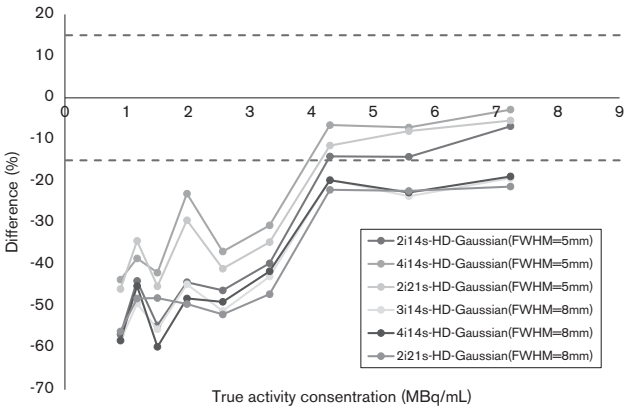

Differences in the measured activity concentration in all syringes with respect to the true activity concentration for various reconstruction parameters over nine imaging time-points. FWHM, full-width at half-maximum.

Table 2 Minimum detectable activity (MBq/ml)

Syringe diameter (mm)	30.5	22	17.5	13.65	9.15[a]
Minimum detectable activity (quantitative assessment)	0.32	1.18	1.53	1.98	3.25
Minimum detectable activity (qualitative assessment)	0.32	0.91	0.91	1.53	5.58

[a]For the smallest syringe, the partial volume effect (PVE) is considered.

However, as the activity concentration of ^{90}Y in tumors, following administration of radioembolization therapy, is of the order of 3 MBq/ml, the proposed diagnostic administration of ^{90}Y is appropriate for lesions whose diameter exceeds 9 mm. As such, PET/CT imaging of low-dose ^{90}Y using the introduced optimized reconstruction parameters, for lesion sizes and activity concentrations above a certain threshold, is feasible.

For the reconstruction parameters optimized for detectability, ^{90}Y MDA from PET/CT image is determined both quantitatively and qualitatively, taking lesion size and activity concentration into account. Table 2 shows the estimated quantitative and qualitative MDA for syringes with various sizes for the mentioned optimized reconstructions. The limit of detectability depends on the shape and size of the lesions. The limit of CNR in this work (i.e. CNR > 8) is chosen according to a study carried out based on human observers [38]. The quantitative results achieved are in good agreement with qualitative assessments. All lesions with activity concentrations exceeding 3.28 ± 10%MBq/ml are detectable irrespective of lesion size. The results achieved are consistent with the results reported by Carlier *et al.* [28] and by Van Elmbt *et al.* [29], in which the selected SBR was one order of magnitude smaller than our study (Table 2).

Quantitative accuracy

Because of statistical fluctuations, the measured activity concentration of a false-positive signal could reach up to a few MBq/ml. In this study, the associated error margins for activity concentrations greater than 4 MBq/ml are limited to −15% for the optimized reconstruction parameters, which are in an acceptable range [39]. For activity concentrations smaller than 4 MBq/ml, the count density decreases noticeably; thus, the magnitude of the measured signal is in the order of the background noise, and as such, quantitative estimation is not reliable. For the evaluated activity concentrations range in this study, the results achieved are in good agreement with previous published data [21,28,39] that consistently underestimated the quantitative measurements.

In this study, postsmoothing filters with various strengths were used to investigate impact on detectability and quantitative accuracy in the reconstructed volumes. The CNR values were significantly improved by implementing Gaussian postsmoothing filters with higher FWHM values as smoother filters resulted in greater noise reduction in the reconstructed images [30].

The results depend significantly on the total detected counts, and accordingly, on the acquisition duration. In this study, the implemented acquisition time of 45 min resulted in an acceptable image intensity for activity concentrations above 4 MBq/ml, whereas for lower activity concentrations, increasing the acquisition time is suggested.

The VOI determination method (using both CT and PET image to determine the syringe boundaries) has a considerable impact on the average measured image intensities. Further increasing the segmented size would negatively affect the VOI average intensity and accordingly detectability and quantitative accuracy. In particular, volume segmentation methods can cause an unavoidable inaccuracy in this context and more researches are required to standardize the method.

Conclusion

In this study, we concluded that ^{90}Y PET/CT imaging, even with a very low activity concentration, is feasible, and is able to depict the distribution of ^{90}Y implanted microspheres above a certain minimum threshold for radioactive concentrations and lesion sizes. For the quantification and detection of lesions, reconstruction parameters were distinctly optimized.

The proposed framework for in-vivo PET/CT imaging of low-dose ^{90}Y in pretherapeutic stage could be viable and may determine the amount of therapeutic activity to be injected to the patients in SIRT using the introduced optimized reconstruction parameters. This method has the significant potential to improve the treatment efficacy if intraoperative PET/CT imaging in SIRT is possible.

Acknowledgements

The authors wish to acknowledge very helpful discussions with Drs Martin Lodge and Eric Frey of Johns Hopkins University.

Conflicts of interest

There are no conflicts of interest.

References

1 Prompers L, Bucerius J, Brans B, Temur Y, Berger L, Mottaghy FM. Selective internal radiation therapy (SIRT) in primary or secondary liver cancer. *Methods* 2011; **55**:253–257.
2 Salem R, Thurston KG. Radioembolization with ^{90}Yttrium microspheres: a state-of-the-art brachytherapy treatment for primary and secondary liver malignancies. Part 1: technical and methodologic considerations. *J Vasc Interv Radiol* 2006; **17**:1251–1278.
3 Dancey JE, Shepherd FA, Paul K, Sniderman KW, Houle S, Gabrys J, *et al*. Treatment of nonresectable hepatocellular carcinoma with intrahepatic ^{90}Y-microspheres. *J Nucl Med* 2000; **41**:1673–1681.
4 Kao YH, Tan EH, Ng CE, Goh SW. Clinical implications of the body surface area method versus partition model dosimetry for yttrium-90 radioembolization using resin microspheres: a technical review. *Ann Nucl Med* 2011; **25**:455–461.
5 Knesaurek K, Machac J, Muzinic M, DaCosta M, Zhang Z, Heiba S. Quantitative comparison of yttrium-90 (^{90}Y)-microspheres and technetium-99m (^{99m}Tc)-macroaggregated albumin SPECT images for planning ^{90}Y therapy of liver cancer. *Technol Cancer Res Treat* 2010; **9**:253–262.
6 Ulrich G, Dudeck O, Furth C, Ruf J, Grosser OS, Adolf D, *et al*. Predictive value of intratumoral ^{99m}Tc-macroaggregated albumin uptake in patients with colorectal liver metastases scheduled for radioembolization with ^{90}Y-microspheres. *J Nucl Med* 2013; **54**:516–522.
7 Wondergem M, Smits ML, Elschot M, de Jong HW, Verkooijen HM, van den Bosch MA, *et al*. ^{99m}Tc-macroaggregated albumin poorly predicts the intrahepatic distribution of ^{90}Y resin microspheres in hepatic radioembolization. *J Nucl Med* 2013; **54**:1294–1301.
8 Ng SC, Lee VH, Law MW, Liu RK, Ma VW, Tso WK, *et al*. Patient dosimetry for 90Y selective internal radiation treatment based on ^{90}Y PET imaging. *J Appl Clin Med Phys* 2013; **14**:212–221.
9 Sarfaraz M, Kennedy AS, Lodge MA, Li XA, Wu X, Yu CX. Radiation absorbed dose distribution in a patient treated with yttrium-90 microspheres for hepatocellular carcinoma. *Med Phys* 2004; **31**:2449–2453.
10 Minarik D, Sjogreen Gleisner K, Ljungberg M. Evaluation of quantitative (^{90})Y SPECT based on experimental phantom studies. *Phys Med Biol* 2008; **53**:5689–5703.
11 Rault E, Vandenberghe S, Staelens S, van Holen R, Lemahieu I. Optimization of Y90 bremsstrahlung image reconstruction using multiple energy window subsets. *J Nucl Med* 2008; **49**:399P.
12 Rong X, Du Y, Ljungberg M, Rault E, Vandenberghe S, Frey EC. Development and evaluation of an improved quantitative ^{90}Y bremsstrahlung SPECT method. *Med Phys* 2012; **39**:2346–2358.
13 Walrand S, Hesse M, Demonceau G, Pauwels S, Jamar F. Yttrium-90-labeled microsphere tracking during liver selective internal radiotherapy by bremsstrahlung pinhole SPECT: feasibility study and evaluation in an abdominal phantom. *EJNMMI Res* 2011; **1**:32.
14 Arley N, Moller C. Uber die innere paar erzeugung biem beta-zerfall. *K Dan Vidensk Selsk Mat Fys Medd* 1938; **15**.
15 Greenberg J, Deutsch M. Positrons from the decay of P-32 and Y-90. *Semin Nucl Med* 1956; **102**:415–421.
16 Selwyn RG, Nickles RJ, Thomadsen BR, DeWerd LA, Micka JA. A new internal pair production branching ratio of ^{90}Y: the development of a non-destructive assay for ^{90}Y and ^{90}Sr. *Appl Radiat Isot* 2007; **65**:318–327.
17 Gates VL, Esmail AA, Marshall K, Spies S, Salem R. Internal pair production of ^{90}Y permits hepatic localization of microspheres using routine PET: proof of concept. *J Nucl Med* 2011; **52**:72–76.
18 Lhommel R, van Elmbt L, Goffette P, van den Eynde M, Jamar F, Pauwels S, *et al*. Feasibility of ^{90}Y TOF PET-based dosimetry in liver metastasis therapy using SIR-spheres. *Eur J Nucl Med Mol Imaging* 2010; **37**:1654–1662.
19 Lhommel R, Goffette P, van den Eynde M, Jamar F, Pauwels S, Bilbao JI, *et al*. Yttrium-90 TOF PET scan demonstrates high-resolution biodistribution after liver SIRT. *Eur J Nucl Med Mol Imaging* 2009; **36**:1696.
20 Walrand S, Jamar F, van Elmbt L, Lhommel R, Bekonde EB, Pauwels S. 4-Step renal dosimetry dependent on cortex geometry applied to ^{90}Y peptide

receptor radiotherapy: evaluation using a fillable kidney phantom imaged by ^{90}Y PET. *J Nucl Med* 2010; **51**:1969–1973.
21 Goedicke A, Berker Y, Verburg FA, Behrendt FF, Winz O, Mottaghy FM. Study-parameter impact in quantitative 90-Yttrium PET imaging for radioembolization treatment monitoring and dosimetry. *IEEE Trans Med Imaging* 2013; **32**:485–492.
22 Rahmim A, Tang J. Noise propagation in resolution modeled PET imaging and its impact on detectability. *Med Phys Biol* 2013; **58**:6945–6968.
23 Richard S, Samei E. Quantitative breast tomosynthesis: from detectability to estimability. *Med Phys* 2010; **37**:6157–6165.
24 Chen B. Predicting Task-specific Performance for Iterative Reconstruction in Computed Tomography, PhD Dissertation, Duke University 2014.
25 Chen B, Ramirez Giraldo Jc, Solomon J, Samei E. Evaluating iterative reconstruction performance in computed tomography. *Med Phys* 2014; **41**:121913.
26 Rahmim A, Qi J, Sossi V. Resolution modeling in PET imaging: theory, practice, benefits, and pitfalls. *Med Phys* 2013; **40**:064301.
27 Alessio A, Rahmim A, Orton CG. Resolution modeling enhances PET imaging (Point/Counterpoint). *Med Phys* 2013; **40**:120601.
28 Carlier T, Eugene T, Bodet-Milin C, Garin E, Ansquer C, Rousseau C, *et al*. Assessment of acquisition protocols for routine imaging of Y-90 using PET/CT. *EJNMMI Res* 2013; **3**:11.
29 van Elmbt L, Vandenberghe S, Walrand S, Pauwels S, Jamar F. Comparison of yttrium-90 quantitative imaging by TOF and non-TOF PET in a phantom of liver selective internal radiotherapy. *Phys Med Biol* 2011; **56**:6759–6777.
30 Goertzen AL, Suk JY, Thompson CJ. Imaging of weak-source distributions in LSO-based small-animal PET scanners. *J Nucl Med* 2007; **48**:1692–1698.
31 Yamamoto S, Horii H, Hurutani M, Matsumoto K, Senda M. Investigation of single, random, and true counts from natural radioactivity in LSO-based clinical PET. *Ann Nucl Med* 2005; **19**:109–114.
32 Watson CC, Casey ME, Eriksson L, Mulnix T, Adams D, Bendriem B. NEMA NU 2 performance tests for scanners with intrinsic radioactivity. *J Nucl Med* 2004; **45**:822–826.
33 Fourkal E, Veltchev I, Lin M, Koren S, Meyer J, Doss M, *et al*. 3D inpatient dose reconstruction from the PET-CT imaging of ^{90}Y microspheres for metastatic cancer to the liver: feasibility study. *Med Phys* 2013; **40**:081702.
34 Bao Q, Chatziioannou AF. Estimation of the minimum detectable activity of preclinical PET imaging systems with an analytical method. *Med Phys* 2010; **37**:6070–6083.
35 Cherry SR, Sorenson JA, ME Phelps. eds. *Physics in nuclear medicine*, 4th ed. Philadelphia: Pennsylvania Elsevier Saunders; 2012.
36 Stute S, Carlier T, Cristina K, Noblet C, Martineau A, Hutton B, *et al*. Monte Carlo simulations of clinical PET and SPECT scans: impact of the input data on the simulated images. *Phys Med Biol* 2011; **56**:6441–6457.
37 Beijst C, Kist JW, Elschot M, Viergever MA, Hoekstra OS, de Keizer B, *et al*. Quantitative comparison of ^{124}I PET/CT and ^{131}I SPECT/CT detectability. *J Nucl Med* 2016; **57**:103–108.
38 Bright DS, Newbury DE, Steel EB. Visibility of objects in computer simulations of noisy micrographs. *J Microsc* 1998; **189**:25–42.
39 Willowson KP, Tapner M, Bailey DL. A multicentre comparison of quantitative (90)Y PET/CT for dosimetric purposes after radioembolization with resin microspheres: The QUEST Phantom Study. *Eur J Nucl Med Mol Imaging* 2015; **42**:1202–1222.
40 Henkin RE, Bova D, Dillehay GL, Halama JR, Karesh SM, Wagner RH, *et al*. *Nuclear medicine (vol 1)*, 2nd ed. Philadelphia, PA: Mosby; 2006.
41 Campbell AM, Bailey IH, Burton MA. Tumour dosimetry in human liver following hepatic yttrium-90 microsphere therapy. *Phys Med Biol* 2001; **46**:487–498.
42 Fox RA, Klemp PF, Egan G, Mina LL, Burton MA, Gray BN. Dose distribution following selective internal radiation therapy. *Int J Radiat Oncol Biol Phys* 1991; **21**:463–467.
43 Kennedy AS, Nutting C, Coldwell D, Gaiser J, Drachenberg C. Pathologic response and microdosimetry of (90)Y microspheres in man: review of four explanted whole livers. *Int J Radiat Oncol Biol Phys* 2004; **60**:1552–1563.